



Analysis of Global Positioning System (GPS) radio occultation measurement errors based on Satellite de Aplicaciones Cientificas-C (SAC-C) GPS radio occultation data recorded in open-loop and phase-locked-loop mode

Martin S. Lohmann¹

Received 6 July 2006; revised 14 November 2006; accepted 18 December 2006; published 10 May 2007.

[1] The error characteristics of Global Positioning System (GPS) radio occultation (RO) measurement errors are studied based on Satellite de Aplicaciones Cientificas-C (SAC-C) GPS radio occultation data tracked in both open-loop (OL) and phase-locked-loop (PLL) mode. The error characteristics are derived by applying dynamical error estimation, i.e., without using any external data. The computed error profiles show that the mean measurement errors are the smallest in the height range between about 5–7 km and 20–25 km, about 0.2–1% for bending angles and 0.1–0.2% for refractivity at all latitudes. The largest measurement errors are found in the lower troposphere, where the mean bending angle measurement errors are within the range from 1 to 6%, whereas the mean refractivity measurement errors are within the range from 0.2% to 1%. From the error distributions, it is found that the occultation-to-occultation variability of the measurement errors generally spans one order of magnitude. The bending angle error correlation length is about 1 km and 100 m, at high and low altitudes, respectively, corresponding approximately to the cutoff frequency of the applied noise filters. The widths of the refractivity error autocorrelation functions are notably broader. The variability and the magnitude of the OL measurement errors are larger than for the PLL measurement errors. This is mainly attributed to the ability of OL tracking to track RO signals under atmospheric conditions for which PLL tracking fails.

Citation: Lohmann, M. S. (2007), Analysis of Global Positioning System (GPS) radio occultation measurement errors based on Satellite de Aplicaciones Cientificas-C (SAC-C) GPS radio occultation data recorded in open-loop and phase-locked-loop mode, *J. Geophys. Res.*, 112, D09115, doi:10.1029/2006JD007764.

1. Introduction

[2] During the last decade or so, the potential of Global Positioning System (GPS) radio occultation (RO) for sounding and monitoring of the Earth's atmosphere has been demonstrated in a number of studies. RO data have been successfully applied to study a wide range of atmospheric processes including gravity wave activity [e.g., *de la Torre and Alexander*, 2005; *Ratnam et al.*, 2004; *Tsuda and Hocke*, 2004], the tropopause [e.g., *Schmidt et al.*, 2005, 2006], and the distribution of water vapor [e.g., *Kursinski and Hajj*, 2001; *Marquardt et al.*, 2001] as well as for validation of other instruments and numerical weather prediction (NWP) models [e.g., *Gobiet et al.*, 2005; *Kuo et al.*, 2004; *Schröder et al.*, 2003]. Furthermore, the potential of RO data for improving weather forecasts has also been demonstrated in recent years [*Healy et al.*, 2005; *Healy and Thépaut*, 2005, 2006; *Zou et al.*, 2004].

[3] According to Snell's law, radio waves propagating through the Earth's atmosphere are bent because of refractivity gradients in the neutral atmosphere and in the ionosphere. This effect is used in the GPS radio occultation technique, where GPS radio waves traversing the Earth's atmosphere are measured by a Low Earth Orbiting (LEO) satellite as this satellite sets behind the earth's limb and thus provides a vertical scan of the atmosphere [*Kursinski et al.*, 1997]. In a spherically symmetric atmosphere, the bending angles of the rays are directly related to the measured Doppler shifts through the occultation geometry. At GPS frequencies, the neutral atmosphere is nondispersive, whereas the ionosphere is dispersive. This allows for reconstruction of the bending angle profiles corresponding to the neutral atmosphere through a linear combination of pairs, corresponding to the two frequencies in the GPS system, of either signal phase [*Spilker*, 1980], phase modulation [*Melbourne et al.*, 1994], bending angle, [*Vorob'ev and Krasil'nikova*, 1994], or Doppler shift [*Ladreitner and Kirchengast*, 1996]. These techniques are commonly referred to as ionospheric calibration or ionospheric correction.

[4] By assuming spherical symmetry in the atmosphere, the ionospheric free bending angle profiles can be inverted

¹Teklatech A/S, Diplomvej, Lyngby, Denmark.

into profiles of refractivity for the neutral atmosphere through the Abel transform [Fjeldbo *et al.*, 1971]. Application of the hydrostatic equation and the equation of state allows for retrieval of so-called dry-temperature profiles, whereas retrieval of specific humidity for GPS occultation requires auxiliary data [e.g., Hajj *et al.*, 2002; Kursinski *et al.*, 1997, 2000].

[5] Being a limb-sounding technique, RO soundings are characterized by a low horizontal and a high vertical resolution. For geometrical optical (GO) processing (that is, direct computation of the atmospheric induced Doppler shift from the measured signal phase), the vertical resolution is limited by diffraction to the size of the Fresnel zone. For radio holographic (RH) processing, the vertical resolution is limited by diffraction within the atmosphere and by the size of the synthetic aperture. At GPS frequencies, the vertical resolution for GO processing is about 0.5–1.4 km [Kursinski *et al.*, 2000], while the vertical resolution for RH processing is about 60 m [Gorbunov *et al.*, 2004], though this resolution is often reduced in practice because of the use of noise filtering. The horizontal resolution L of RO may be defined by the distance traversed by the radio path as it enters and exits a layer having vertical resolution H ; in this case, the horizontal and vertical resolution may be related as $L \approx 2(2r_e H)^{1/2}$, where r_e is the Earth's radius [Kursinski *et al.*, 2000]. Consequently: $H = 0.06\text{--}1\text{ km} \Rightarrow L = 50\text{--}200\text{ km}$.

[6] RO measurement errors arise from instrumental errors (local multipath, i.e., unwanted RO signals scattered off the spacecraft near the antenna, and thermal noise), atmospheric effects (scintillations caused by small non-spherically symmetric irregularities of refractivity and residual errors from the ionospheric calibration of the occulted signals and the reference links), and retrieval errors (errors related to statistical optimization (SO) and unresolved multipath propagation).

[7] The resolution and the measurement errors impose fundamental limits on the accuracy and the precision to which atmospheric structures can be detected by the RO technique. Reliable estimates of the resolution and the measurement errors are therefore of great importance for the application of RO data whether it is for studying a particular atmospheric phenomenon, for validation of another instrument, or for data assimilation into an NWP model. For instance, Marquardt and Healy [2005] demonstrated the importance of considering the limits imposed by measurement noise when studying gravity wave characteristics from RO observations.

[8] Whether resolution or measurement noise or both are the limiting factor depends on the particular application. Here it is worth noting that NWP models contain only a limited spectrum of the atmospheric circulations, which results in additional differences between RO data and a given NWP model. In a data assimilation scheme, such differences are included in the observation errors. These differences may be significantly larger than the differences caused by the RO resolution and the RO measurement errors. This is particularly the case for the tropical stratosphere due to the significant gravity wave activity in that region of the atmosphere [Healy and Thépaut, 2006].

[9] The error statistics for RO data have been evaluated in a number of studies. Kursinski *et al.* [1997, 2000] performed a thorough study of different RO error sources based

on first-order statistics deriving complete error budgets for retrieved refractivity, geopotential height, and temperature. Rocken *et al.* [1997] evaluated the accuracy and the precision of RO observations by comparing observations from the GPS/Meteorology Microlab-1 (GPS/MET) satellite with correlative data from NWP models, radio sonde observations, and the Geostationary Operational Environmental Satellite System (GOES), Television Infrared Observation Satellite Program Operational Vertical Sounder (TOVS), Upper Atmosphere Research Satellite (UARS)/Microwave Limb Sounder (MLS), and Halogen Occultation Experiment (HALOE) orbiting atmospheric sensors. Steiner *et al.* [1999] assessed the quality of GPS/MET RO data by employing a Monte Carlo technique and by comparing the GPS/MET RO data to the analysis from the European Centre for Medium-Range Weather Forecasts (ECMWF). Syndergaard [1999] computed measurement error statistics for bending angle, refractivity, pressure, and temperature based on an error covariance analysis. A similar study was performed by Rieder and Kirchengast [2001] using Bayesian error analysis. Gorbunov and Kornblueh [2003] evaluated RO measurement errors from the GPS/MET and the Challenging Minisatellite Payload (CHAMP) satellites by comparing RO and ECMWF data based on forward modeling and inversion of artificial radio occultation data. Kuo *et al.* [2004] estimated RO measurements errors for the CHAMP and the Satellite de Aplicaciones Cientificas-C (SAC-C) RO missions by comparing measured refractivities to corresponding refractivities from a forecast and by jointly estimating the forecast errors. In that study, measurement errors were also assessed by comparing soundings that fall within 300 km and 2 hours from each other. Hajj *et al.* [2004] assessed the precision and accuracy of RO measurements by comparing dry-temperature profiles between pairs of CHAMP and SAC-C occultations occurring within 30 min and 200 km of one another. Steiner and Kirchengast [2005] computed error statistics for RO retrievals of bending angle, refractivity, temperature, pressure, and specific humidity based on simulations. Gorbunov *et al.* [2006] presented a technique for dynamic error estimation for RO data and applied this technique to 90 CHAMP occultations to produce a global statistic of RO dry-temperature measurement errors.

[10] Though the statistical properties of RO measurement errors can be estimated as a function of latitude and even season, such error estimates cannot distinguish between the large variations in the magnitude of the RO measurement errors between different occultations.

[11] In this study, we apply dynamic error estimation to SAC-C RO data in order to investigate RO measurement error characteristics including occultation-to-occultation variations, mean error profiles, and error correlation lengths.

[12] Error characteristics are presented for both bending angles and refractivities. Tropospheric error characteristics for occultations where the GPS signals are tracked by the traditional phase-locked-loop (PLL) tracking technique [Stephens and Thomas, 1995] are compared with the error characteristics for occultations where the GPS signals are tracked using the alternative open-loop (OL) tracking technique [Hajj *et al.*, 2004; Sokolovskiy, 2001, 2004; Sokolovskiy *et al.*, 2006b]. For the stratosphere and middle and upper troposphere, errors are computed dynamically by applying the error estimation techniques presented by Lohmann [2005,

2006]. For the lowest troposphere where RO signals generally are very noisy, a simple technique is presented for dynamic estimation of the RO measurement errors.

[13] The study is restricted to random errors, and no attempt is being made to assess biases in the RO data. Biases in RO observation may arise from the climate model used for SO (at high altitudes), unresolved multipath propagation (in the moist troposphere), the presence of so-called super-refraction layers in the moist troposphere, which causes refractivity biases [Ao *et al.*, 2003; Sokolovskiy, 2003], tracking errors [Ao *et al.*, 2003; Beyeler *et al.*, 2003] (for PLL tracking), and early signal truncation [Sokolovskiy, 2003] (for PLL tracking).

[14] The data used in this study have been processed by University Corporation for Atmospheric Research (UCAR)'s Cosmic Data Analysis and Archive Center (CDAAC) RO processing system.

[15] This study is organized into the following form. Section 2 gives an overview of the current CDAAC processing system. Section 3 presents the methodology applied to estimate the RO measurement errors. In section 4, different statistical properties of the errors are presented for both OL and PLL occultations. Finally, Section 5 summarizes the findings and conclusions of this study.

2. CDAAC Data Processing Procedures

[16] Kuo *et al.* [2004] give a thorough description of CDAAC processing procedures. In this section, only a brief overview of CDAAC processing procedures will be given with the main emphasis on later modifications to CDAAC's statistical optimization scheme, which are not described by Kuo *et al.* [2004].

[17] Occultation data processed by CDAAC can be divided into two separate regions, where different data processing strategies are applied; these are the GO region, where GO processing is used SO is applied for the retrieval of refractivity, and the RH region, where RH processing is used.

2.1. GO Region

[18] The GO region covers the interval from the top of the occultation down to the lowest height for which the L2 signal can be tracked. For SAC-C OL tracking, L2 tracking is always terminated when the L1 OL tracking is turned on at a height of about 10 km, if tracking has not already been stopped at higher altitudes, since the Black Jack GPS receiver onboard the satellite is not capable of simultaneous tracking of both L2 and L1 in OL mode.

[19] In the GO region, bending angles are computed from the L1 and L2 phase data and ionospheric calibration is performed as a linear combination of the L1 and L2 bending angles. Smoothing is applied to the L1 and L2 phases in the form of a Fourier filter with a Gaussian-shaped window function for the spectrum. The resulting resolution of the ionospheric free bending angles is approximately 1 km, consistent with the size of the Fresnel zone at the mean height of the tropopause.

[20] SO is applied to reduce the impact of high-altitude bending angle errors on the retrieved refractivities at lower altitudes. SO is based on a statistical optimal combination of the measured bending angle profiles and First Guess bend-

ing angle profiles [see e.g., Gorbunov *et al.*, 1996; Healy, 2001]. The First Guess profiles are commonly derived from a climate model. The CDAAC SO scheme is based on dynamical error estimation of both measurement errors and First Guess errors as described by Lohmann [2005].

[21] The climate model currently used by CDAAC for SO is an National Center for Atmospheric and Climate Research (NCAR) climate model based on the results from the Stratospheric Processes and Their Role in Climate (SPARC) study [Randel *et al.*, 2002].

[22] In SO, errors from the climate model can be greatly reduced if the climate model bending angle profiles are adjusted properly to the measured bending angles before they are used as First Guess [Gobiet and Kirchengast, 2004; Gorbunov, 2002b; Lohmann, 2005]. In CDAAC processing, different adjustment schemes can be used; in this study, the climate model bending angles are adjusted by scaling the amplitude and the scale height, i.e.,

$$\alpha_g(a) = A\alpha_c(a)^B \quad (1)$$

where a is the impact parameter and α_c and α_g represent the climate model bending angles and the First Guess bending angles, respectively. The two scaling factors, A and B , are computed for each occultation by minimizing:

$$\sum_i [\ln(\alpha_{ms}(a_i)) - \ln(A) - B \ln(\alpha_c(a_i))]^2 \quad (2)$$

where α_{ms} represents the heavily smoothed (over about 5 km) measured bending angle profile. Heavy smoothing is applied to stabilize the estimates of A and B as originally suggested by Gorbunov [2002b]. Even with heavy smoothing, the $\ln(\alpha_{ms})$ profiles fluctuate considerably at high altitudes, where the measurement noise is dominating. To prevent noise at high altitudes from degrading the estimates of A and B , equation (2) is applied only in the height interval from 20 km up to the height, z_{max} , where the deviations between α_{ms} and the ionospheric free bending angles, smoothed over approximately 1 km, exceed 60%. The lower height limit is set to 20 km since CDAAC does not use SO below that height. Above z_{max} , the First Guess is computed as a smooth transition between the modified and the original climate model profile in the height range from 60 km down to z_{max} . Hence the First Guess is always identical to the climate model above 60 km.

[23] The optimized bending angles α_o are computed as a linear combination of the measured bending angle profile α_m and α_g as:

$$\alpha_o = \alpha_g - w\Delta\alpha, \quad \Delta\alpha = \alpha_m - \alpha_g \quad (3)$$

The weighting factor w is a function of the measurement error standard deviation σ_m , the First Guess error standard deviation σ_g , and the corresponding error correlation length l_m and l_g . w is computed as [Lohmann, 2005]:

$$w = \left(1 + \frac{\sigma_m^2}{\sigma_g^2} \left(\frac{l_m}{l_g} \right)^{0.82} \right)^{-1} \quad (4)$$

The methodology used for estimation of σ_m , σ_g , l_m , and l_g is described in section 3.

2.2. RH Region

[24] The RH region extends from the lowest height to which the L2 signal can be tracked down to the lowest point in the occultation profile. Bending angles are computed from the L1 complex signal using full spectrum inversion (FSI) [Jensen *et al.*, 2003], with correction for noncircular orbits performed by geometrical optical propagation to a nearby perfect circular orbit [Sokolovskiy, 2004]. Pairs of impact parameter a and bending angles α are computed as:

$$a = \frac{\omega}{k \frac{d\theta}{dt}} \quad (5)$$

$$t(a) = -\frac{d \arg(F)}{d\omega} \quad (6)$$

$$\alpha(a) = \theta + \text{asin}\left(\frac{a}{r_{\text{TX}}}\right) + \text{asin}\left(\frac{a}{r_{\text{RX}}}\right) - \pi \quad (7)$$

in which:

- F is the FSI-transformed RO signal.
- ω is the angular frequency in radians.
- k is the wave number of the GPS signal.
- t is time.
- r_{TX} is the distance from the local center of curvature to the transmitter/GPS satellite.
- r_{RX} is the distance from the local center of curvature to the receiver/LEO satellite.
- θ denotes the angle between the two satellite radius vectors.

[25] To suppress noise, the retrieved bending angles are smoothed with a running median filter followed by a running average filter. After noise filtering, the resulting resolution of the FSI retrieved bending angles is about 100 m. Ionospheric calibration in the RH region is performed by assuming that the correction to the L1 bending angle in the ionospheric calibration is constant below the height where L2 is lost.

3. RO Error Estimation

[26] Different error estimation procedures are applied in the GO region and in the RH region because of the different processing strategies and the different error sources in the two regions.

3.1. GO Region

[27] The region of the atmosphere that is sounded using GO processing is a very dry region, where there is virtually no contribution to the measurement errors from scintillation caused by the neutral atmosphere. The dominant bending angle measurement errors are the instrumental errors and the residual errors from the ionospheric calibration. For refractivity, there is an additional contribution to the measurement errors from the First Guess applied for SO.

[28] The methodology applied in this study for estimation of the measurement errors in the GO region is based on the study of Lohmann [2005]; here only a brief outline is presented, and the reader is referred to that study for further details.

[29] Below the E -layer, the magnitude and structure of the bending angle measurement errors are fairly uniform [Kuo *et al.*, 2004; Kursinski *et al.*, 1997]. Hence if the measurement errors can be computed for one height interval below the E -layer, these errors will be representative for the entire GO region below the E -layer. The height range just below the E -layer is particularly useful for estimation of the measurement errors as the bending caused by the neutral atmosphere is small compared with the measurement errors in that region.

[30] This allows us to consider deviations between measured bending angles and the First Guess bending angles as measurement errors in the height interval just below the E -layer. From these deviations, the standard deviation [Kuo *et al.*, 2004; Sokolovskiy and Hunt, 1996], the error autocorrelation function r_m , and the error correlation length [Lohmann, 2005] of the measurement errors can be computed.

[31] The error estimation approach described above relies on the assumptions that the ionospheric noise from the E -layer and the bending caused by the neutral atmosphere are small compared with the measurement errors in the GO region. Therefore care must be taken when choosing the height interval used for computing the measurement errors. If this height interval is too close to the E -layer, the magnitude of the computed measurement errors will be too large. Similarly, if the interval is too low, the differences between the First Guess and the measurements will be dominated by the errors in the First Guess and the magnitude of the computed measurement errors will also be too large.

[32] In this study, error characteristics for the bending angle measurement errors are computed from the 20 km height interval between 30 and 80 km, where the root mean square deviation between the First Guess and the measured bending angles is the smallest. This approach is applied to find the height interval where the combined contribution to the RMS deviation from the E -layer and the signal from the neutral atmosphere is the smallest. Though the measurement noise can be assumed to be constant below the E -layer, the measurement errors will, however, increase with decreasing height because of defocusing of the RO signals in the lower stratosphere and the troposphere. Defocusing of the RO signals results in increased measurement errors for two reasons: (1) There is a reduction in the signal-to-noise ratio (SNR); (2) at heights where defocusing of RO signals is significant, the gradients in the bending angle profiles are also significant, which leads to an increased uncertainty in the retrieved bending angles as errors in the impact parameter originating from the phase data become important [Syndergaard, 1999].

[33] To account for the reduction in SNR with height, we will apply a first-order approximation and assume that the measurement error variance is inversely proportional to the power SNR, i.e., to the squared L1 voltage SNR, $\text{SNR}_{v,L1}$.

[34] As demonstrated by *Syndergaard* [1999], one can account for the additional uncertainty introduced by errors in the impact parameter by first computing the bending angle error variance, disregarding the errors in the impact parameter, and subsequently multiplying this variance by the ζ^2 , where ζ is the defocusing factor defined as:

$$\zeta = \left| 1 - \frac{D_{\text{TX}}D_{\text{RX}}}{D_{\text{TX}} + D_{\text{RX}}} \frac{d\alpha}{da} \right|^{-1} \quad (8)$$

in which D_{TX} and D_{RX} are distances from the limb to the transmitting and the receiving satellites, and $d\alpha/da$ is the gradient of the bending angle profile w.r.t. impact parameter.

[35] At GPS frequencies where the atmospheric absorption is negligible, the defocusing factor is almost proportional to $(\text{SNR}_{v,L1})^2$. Hence to compute the height-depending measurement error variance σ_m^2 , the total error-enhancing effect of the signal defocusing can approximately be accounted for by scaling the bending angle error variance estimated at high altitudes σ_u^2 as:

$$\sigma_m^2(a) \approx \left(\frac{\text{SNR}_{v,L1}^U}{\text{SNR}_{v,L1}(a)} \right)^6 \sigma_u^2 \quad (9)$$

where $\text{SNR}_{v,L1}^U$ is the $\text{SNR}_{v,L1}$ corresponding to the height interval from which σ_u^2 is computed and $\text{SNR}_{v,L1}(a)$ is the L1 voltage SNR at impact parameter a .

[36] Estimation of the refractivity measurement error variance $\sigma_{N_m}^2$ is more complicated because of the application of SO since the errors of the First Guess used for SO must be estimated in order to compute the total refractivity observation error.

[37] By assuming that the First Guess errors correspond to a fixed fraction K of the First Guess bending angles, the variance σ_g^2 and the autocorrelation function r_g can be computed as [*Lohmann*, 2005]:

$$\sigma_g^2(a) = K^2 \alpha_g^2(a), \quad K^2 = \frac{\sum_i [(\Delta\alpha(a_i))^2 - \sigma_m^2]}{\sum_i \alpha_g^2(a_i)} \quad (10)$$

and

$$\frac{r_g(\tau)}{r_g(0)} \approx \frac{\sum_i [\Delta\alpha(a_i)\Delta\alpha(a_i + \tau) - r_m(\tau)]}{K^2 \sum_i \alpha_g(a_i)\alpha_g(a_i + \tau)} \quad (11)$$

In equation (11), r_m is the autocorrelation function for the measurement bending angle errors.

[38] In CDAAC, equations (10) and (11) are applied in the same height range as equation (2). By assuming Gaussian autocorrelation functions for the First Guess errors and for the measurement errors, the error covariance matrices for the First Guess errors \mathbf{E}_g and the measurement errors \mathbf{E}_m can be expressed as:

$$\mathbf{E}_{g,i,j} = K^2 \alpha_g(a_i)\alpha_g(a_j) \exp\left(-\left(\frac{a_j - a_i}{l_g}\right)^2\right) \quad (12)$$

and

$$\mathbf{E}_{m,i,j} = \sigma_m(a_i)\sigma_m(a_j) \exp\left(-\left(\frac{a_j - a_i}{l_m}\right)^2\right) \quad (13)$$

[39] In equations (12) and (13) the error correlation lengths l_g and l_m are computed through a Gaussian fit to r_g and r_m .

[40] From equation (3), it follows that the error covariance matrix for the optimized bending angle profile is related to the error covariance matrices for the First Guess errors and the measurement errors through:

$$\mathbf{E}_o = \mathbf{E}_g - \mathbf{W}(\mathbf{E}_m - \mathbf{E}_g)\mathbf{W} \quad (14)$$

where \mathbf{W} is a diagonal matrix with diagonal elements $w(a_i)$ as defined by equation (4). Following *Syndergaard* [1999], the covariance \mathbf{E}_N of the refractivity errors are computed as:

$$\mathbf{E}_N = \mathbf{R}\mathbf{E}_o\mathbf{R}^T \quad (15)$$

with:

$$\mathbf{R}_{i,j} = \left[1 + r_i \frac{d(n-1)}{dr} \right]_i \mathbf{A}_{i,j} \quad (16)$$

In equation (16), \mathbf{A} represents the discretized Abel transform and r and n is the radius from the center of sphericity and refractivity index, respectively. The term in the square bracket accounts for errors in r . Equation (16) is different from the corresponding expression given by *Syndergaard* [1999] as there is a typo in that study in the expression for \mathbf{R} (*Syndergaard*, 2006, personal communication).

[41] The variance of the refractivity measurement errors is contained within the diagonal of \mathbf{E}_N thus:

$$\sigma_{N_m}^2(a_i) = \mathbf{E}_{N,i,i} \quad (17)$$

3.2. RH Region

[42] The RH region is characterized by multipath propagation because of humidity structures, which also result in strong scintillations in the RO signals particularly in the lower troposphere. Instrumental noise and residual ionospheric errors may also be important in the upper part of the RH region. Though FSI efficiently resolves multipath propagation in a spherically symmetric atmosphere, this is not necessarily the case in a non-spherically symmetric atmosphere as the bending angle may become a multivalued function of the impact parameter [see e.g., *Gorbunov*, 2002a]. In these cases, the transformed field will suffer from interference from the unresolved multipath propagation, which results in errors in the retrieved bending angles.

[43] Scintillations, unresolved multipath propagation, and instrumental noise introduce a random component in RO signals. RO signals can, thus, be viewed as the sum of a coherent and an incoherent component. Consequently, the FSI-transformed signal may also be considered as being the sum of a coherent and an incoherent component, where the coherent component has constant amplitude. Here we

define the SNR_{FSI} as the power ratio between the coherent and the incoherent part of the FSI-transformed signal.

[44] For $\text{SNR}_{\text{FSI}} > 5$, a time series of bending angle errors $\Delta\alpha_\chi$ may be computed from the FSI log amplitude χ as [Lohmann, 2006]:

$$\Delta\alpha_\chi = -\frac{d\chi}{d\omega} \frac{d\theta}{dt} \quad (18)$$

[45] These bending angle error estimates are uncorrelated with the ‘true’ bending angle errors but have approximately the same statistical properties as the ‘true’ errors [Lohmann, 2006].

[46] In the lower troposphere where scintillations are significant, particularly in the tropics, $\text{SNR}_{\text{FSI}} < 5$, which results in saturation of the log-amplitude fluctuations and, consequently, in underestimation of the bending angle errors estimated from equation (18). To avoid underestimation of the bending angle errors in the lower troposphere, an alternative error estimation procedure is applied below impact heights, where $\text{SNR}_{\text{FSI}} < 5$. Since this region is characterized by relative large errors, the fluctuations in the measured bending angle profile are dominated by noise rather than by atmospheric structures. To estimate the measurement errors, we will, therefore, simply assume that all small-scale bending angle structures are caused by measurement errors. Another synthetic time series of the measurement error can then be computed as:

$$\Delta\alpha_s = \alpha - \alpha_s \quad (19)$$

here α_s is a bending profile computed from t_s where t_s is the ray arrival time computed from equation (6) using 200-m smoothing in the impact parameter domain. Smoothing is implemented through differentiation of the FSI phase by the covariance estimator [Miller and Rochwarger, 1972] as:

$$t_s = -\frac{1}{\delta\omega} \arg \left(\sum_i F(\omega_i) \overline{F(\omega_{i-1})} \right) \quad (20)$$

where $\delta\omega$ is the spectral resolution and overbar represents complex conjugate. The spectral resolution is determined by the length of the time series used for the Fourier transform in the FSI and corresponds to roughly 1 m vertical resolution in the CDAAC processing. The length of the smoothing interval was estimated based on simulations with both additive noise and multiplicative noise. However, the noise characteristic is not very important, what really matters is the structure of the true profile; smoothing intervals longer than 200 m were found to result in an overestimation of the errors, particularly when the ‘true’ bending angle profile has many small-scale structures, whereas shorter smoothing intervals resulted in underestimation of the errors.

[47] The $\Delta\alpha_s$ time series is appended to the $\Delta\alpha_\chi$ time series at the largest impact parameter, where $\text{SNR}_{\text{FSI}} < 5$. SNR_{FSI} is computed from the variance of the FSI log amplitude σ_χ^2 as [Lohmann, 2006]:

$$\text{SNR}_{\text{FSI}} = \frac{1}{2\sigma_\chi^2} \quad (21)$$

Finally, the same median and running average filters as are used for smoothing of the FSI bending angles are applied to the synthetic error time series. From these smoothed errors, one can now compute the relevant error characteristics for the retrieved bending angle profiles.

[48] Refractivity errors in the RH region may be split into two contributions: (1) a contribution from the bending angle errors in the RH region; (2) a contribution from the bending angle errors in the GO region, which propagate to refractivity errors in the RH region through the Abel transform. By assuming that these two error sources are uncorrelated, the total refractivity error variances can be calculated by adding the error variances of these two contributions in the RH region.

[49] In order to generate a new synthetic time series of refractivity errors, from which the contribution from the bending angle errors in the RH region can be computed, the Abel transform is applied to the synthetic bending angle errors throughout the RH region.

[50] The variance of the contribution from bending angle errors in the GO region is computed by applying equation (15) for the entire profile, with $\sigma_m(a) = 0$ in the RH region. The errors computed in this way for the RH region can then be added to the refractivity errors originating from bending angle errors in the RH region.

3.3. Example

[51] To illustrate how the error estimation techniques described above work, Figures 1 and 2 show profiles of retrieved bending angles and refractivities, and corresponding error profiles for two SAC-C occultations with OL tracking below approximately 10 km. For comparison, the retrieved refractivities are plotted together with corresponding refractivity profiles from an ECMWF reanalysis interpolated to the same times and locations as the two occultations.

[52] The most notable feature of the estimated bending angle errors is the abrupt increase in errors at impact heights of about 10 (Figure 1) and 18 km (Figure 2). This increase in the errors marks the transition from the GO region to the RH region and is mainly caused by the reduced smoothing applied in the RH region. Because of the inherent smoothing by the Abel transform, this step-function-like increase in the errors is greatly reduced in the refractivity error profiles. The reason for this is that the bending angle errors in the RH region are reduced more by the Abel transform than the bending angle errors in the GO region because of the different degree of smoothing applied in the two regions. For both occultations, the fractional errors decrease approximately exponentially with height, down to a height of about 10 km, except for the abrupt increase in errors at the GO to RH transition height in Figure 2. Below 10 km, scintillations become important, leading to a decrease in the fractional errors with height and less smooth error profiles. For the two occultations, the fractional bending angle errors span approximately two orders of magnitude, with the smallest errors (about 0.1%) in the lowest stratosphere and upper troposphere and the largest errors (about 10%) in the lower troposphere. For the refractivities, the smallest errors are in the upper troposphere (about 0.2–0.5%) and the largest errors in the lower troposphere (about 1%). For both occultations, excellent agreement is found between retrieved refractivities and the ECMWF analysis.

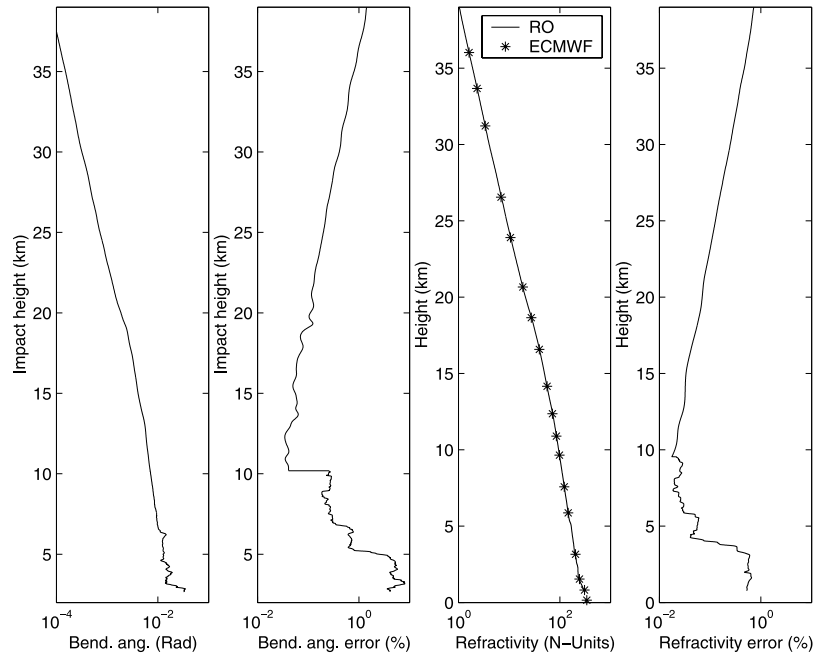


Figure 1. SAC-C occultation, 30 April 2005, 14.34 UTC, 24°S–82°W. First panel: retrieved bending angles, second panel: estimated bending angle errors, third panel: retrieved refractivities and corresponding ECMWF refractivities, fourth panel: estimated refractivity errors.

[53] Figures 3 and 4 show the corresponding SNR_{FSI} profiles. For both occultations, the SNR_{FSI} drops rapidly below approximately 8 km and the SNR_{FSI} estimates become saturated below an impact height of approximately 5 km, implying that the FSI-transformed signals are almost completely incoherent in that region. It is worth noting that, despite of the very low SNR_{FSI} in the lower troposphere, the

retrieved refractivities are in very good agreement with the ECMWF refractivity profiles in that region.

[54] The increase in SNR_{FSI} at 14 km, in Figure 3, coincides fairly well with the tropopause height for this occultation and indicates that, for this occultation, the RO signal experiences stronger scintillations in the lower stratosphere than in the upper troposphere. The drop in SNR_{FSI}

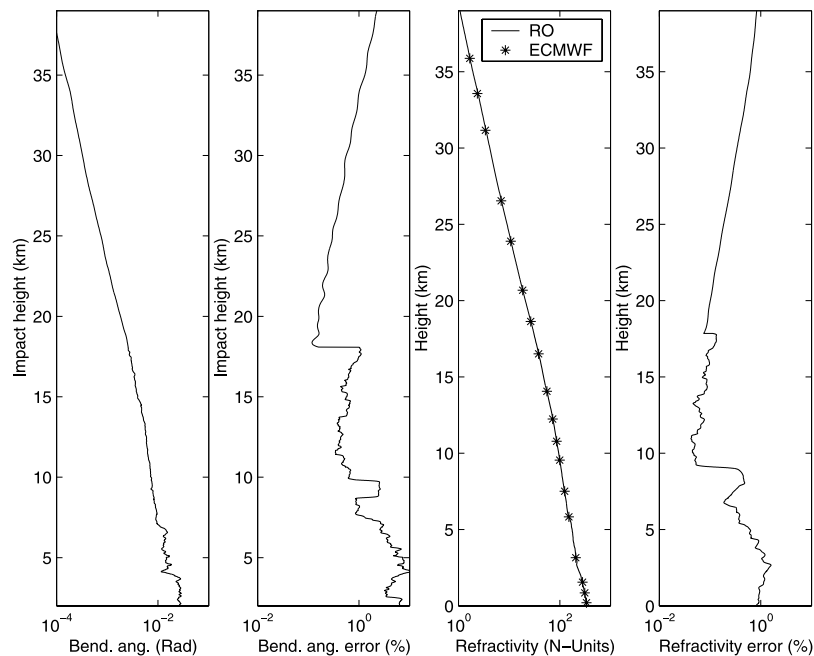


Figure 2. SAC-C occultation, 2 May 2005, 11.26 UTC, 30°S–178°W. First panel: retrieved bending angles, second panel: estimated bending angle errors, third panel: retrieved refractivities and corresponding ECMWF refractivities, fourth panel: estimated refractivity errors.

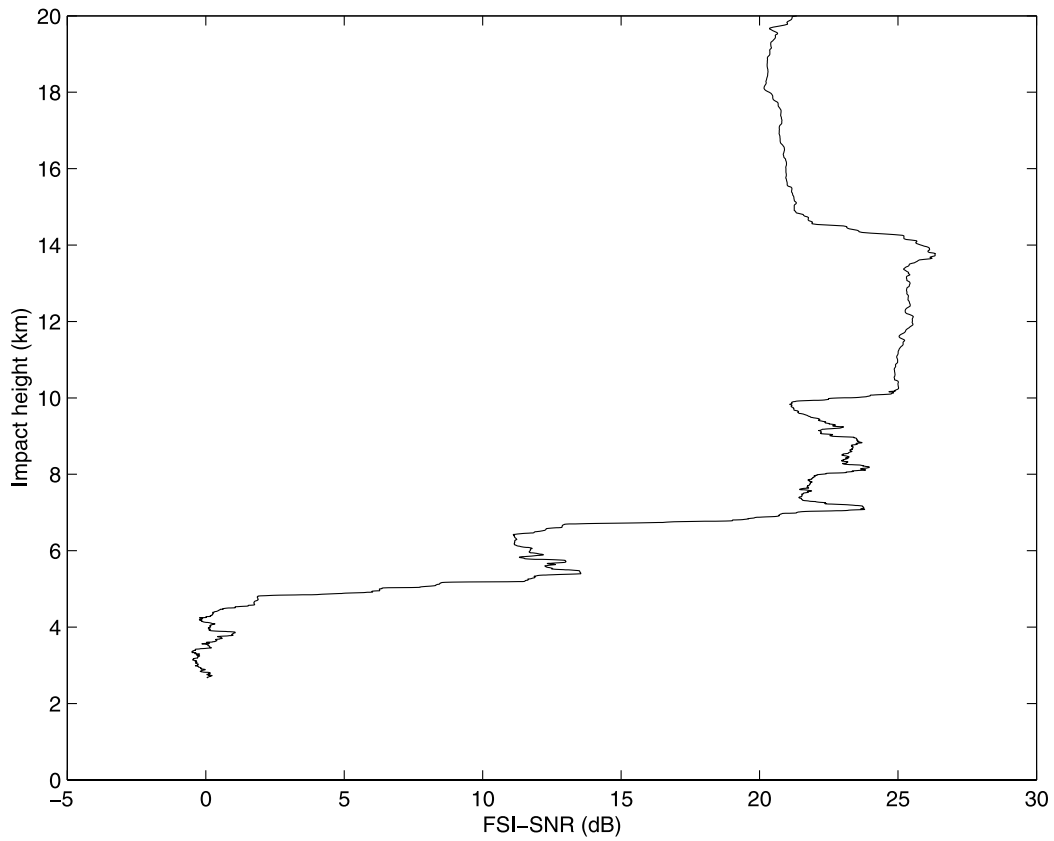


Figure 3. SNR_{FSI} profile, SAC-C occultation, 30 April 2005, 14.34 UTC, 24°S–82°W.

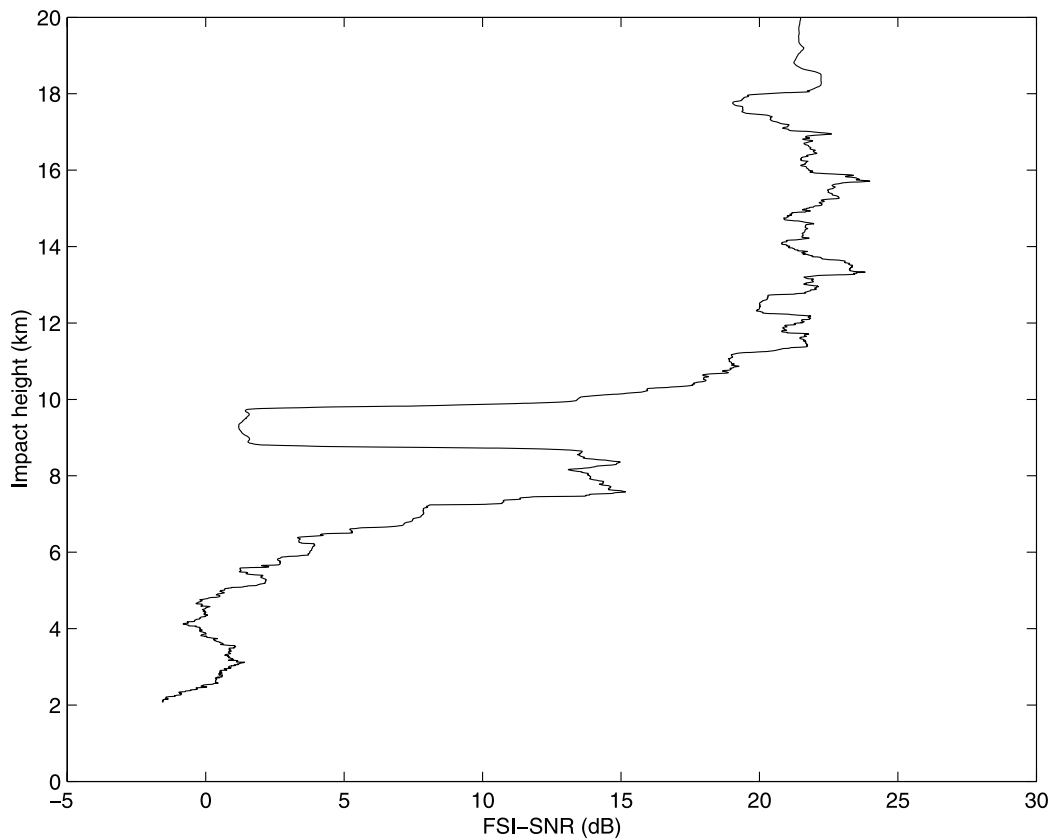


Figure 4. SNR_{FSI} profile, SAC-C occultation, 2 May 2005, 11.26 UTC, 30°S–178°W.

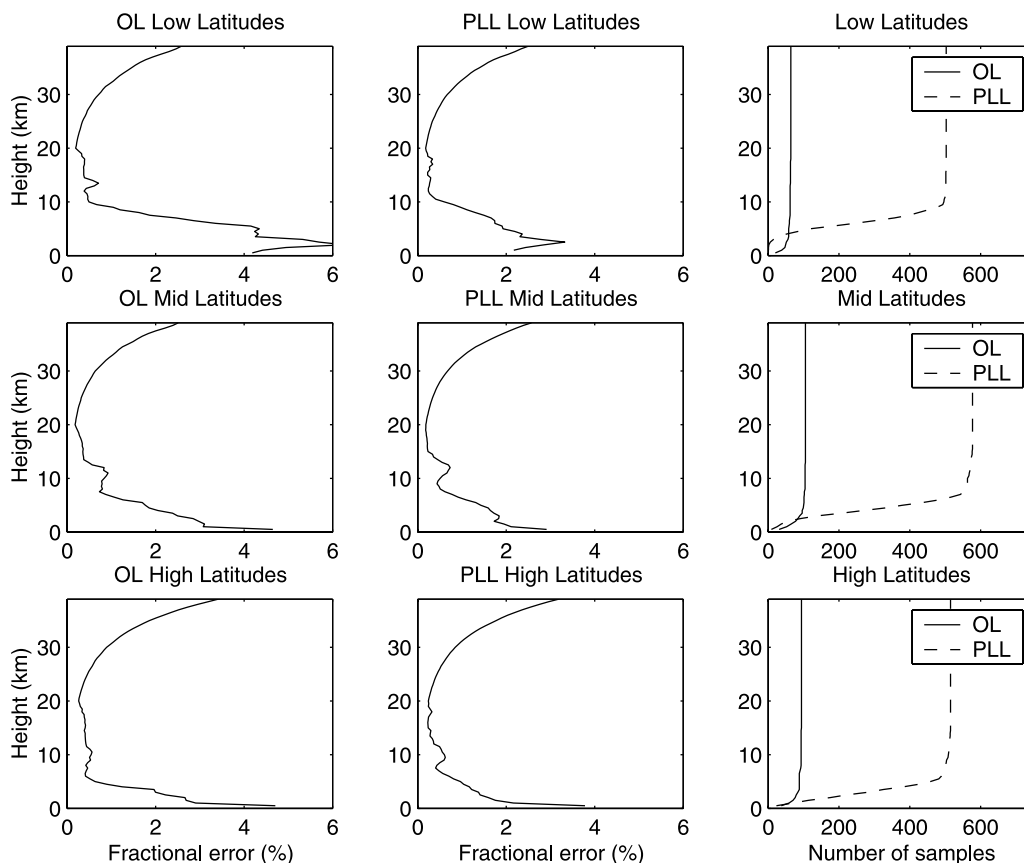


Figure 5. Estimated mean bending angle errors SAC-C RO data from 16 March to 16 May 2005. Left panels: OL tracking below 10 km. Center panels: PLL tracking only.

at 10 km coincides with the height where the receiver loses track of the L2 signal and is probably related to increased scintillations caused by small humidity structures in the midtroposphere. The significant drop in SNR_{FSI} around 10 km height, in Figure 4, is probably caused by some atmospheric layer that causes increased scintillations at that height.

4. Measurement Error Characteristics

[55] In order to investigate the statistical properties of RO measurement errors, the techniques described in the previous section are applied to OL and PLL SAC-C occultations collected by Jet Propulsion Laboratory from 16 March to 16 May 2005. The OL data used in this study were processed using the so-called internal navigation data bit removal [Sokolovskiy *et al.*, 2006b].

4.1. Mean Error Profiles

[56] Figures 5 and 6 depict respectively the mean estimated bending angle error standard deviation profiles and the mean refractivity error standard deviation profiles for three latitude bands in the tropics and the Northern Hemisphere; these are low latitudes (30°S – 30°N), midlatitudes (30°N – 60°N), and high latitudes (60°N – 90°N). Error profiles are presented for PLL tracking as well as for occultations, with OL tracking below 10 km.

[57] Both refractivity errors and bending angle errors are averaged according to their ray tangent height as averaging

according to ray impact parameter is not straightforward because of the Earth's oblateness. Bending angle errors are therefore depicted as a function of ray tangent height rather than as a function of ray impact parameter. This also facilitates comparison between refractivity error profiles and bending angle error profiles.

[58] For comparison, profiles of the fractional standard deviation between OL and PLL refractivity profiles and the ECMWF reanalysis are included in Figure 6; in the following, we will refer to these deviations as the total errors. The ECMWF model field has 21 pressure levels and 2.5° horizontal resolution (~ 225 km). The ECMWF refractivity profiles are derived by interpolating the model field to the same times and locations as the corresponding RO profiles. The statistics for the deviations between PLL and OL data and ECMWF in Figure 6 are similar to results presented by Sokolovskiy (presentation given at AGU Fall Meeting, 2005).

[59] It is important to note that the total errors are not only made up of measurement errors; there are also significant contributions from model errors and representativeness errors arising from differences between model resolution and the RO resolution. For instance, Sokolovskiy *et al.* [2005] demonstrated that there is a strong correlation between a model's horizontal resolution and the deviations between the model and RO data. Furthermore, models contain only a limited spectrum of the atmospheric circulation, and this also contributes to the total errors. Conse-

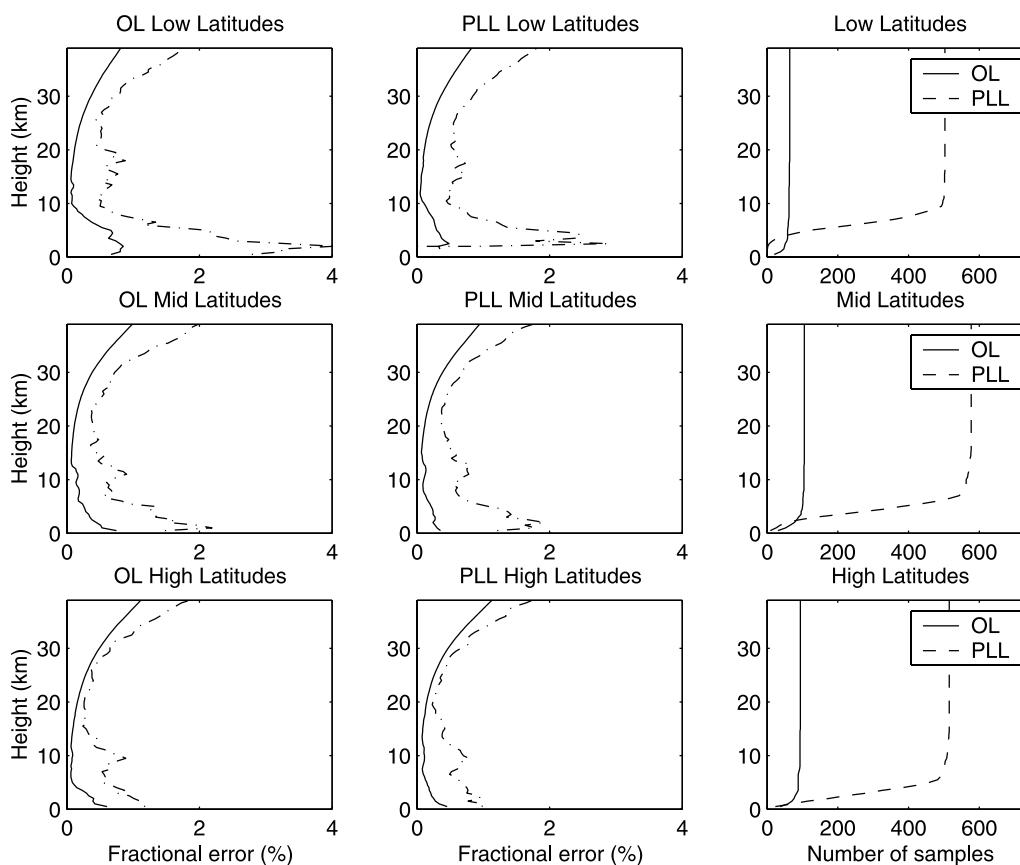


Figure 6. Estimated mean refractivity errors (solid lines) vs. SAC-C minus ECMWF differences (dot-dashed lines), data from 16 March to 16 May 2005. Left panels: OL tracking below 10 km. Center panels: PLL tracking only.

quently, the magnitude of the total errors is strongly dependent upon the given model. The scope of this study is to investigate error characteristics of RO measurement errors, which are by nature independent of the model. However, a discussion of the dominant contributions to the total errors shown in Figure 6 will also be given in the following.

[60] The mean error profiles, in Figures 5 and 6, show that the largest measurement errors are found in the lower troposphere, where the bending angle measurement errors are within the range from 1 to 6% whereas refractivity measurement errors are within the range from 0.2% to 1%.

[61] The measurement errors are the smallest in the height range between about 5–7 km and 20–25 km, about 0.2–1% for bending angles and 0.1–0.2% for refractivity at all latitudes for both OL (only relevant below 10 km) and PLL. Between approximately 20 and 40 km height, the fractional measurement errors increase almost exponentially to approximately 2.5–3% for bending angles and 0.8–1.1% for refractivity.

[62] Generally, OL measurement errors are somewhat larger than the PLL measurement errors, but the OL occultations also have significantly better penetration, especially in the tropics. The higher OL measurement errors combined with the better penetration by the OL can be explained by the ability of the OL to track RO signals under any atmospheric conditions, whereas PLL tracking fails when the atmosphere

contains complex refractivity structures (Sokolovskiy, presentation given at AGU Fall Meeting, 2005).

[63] It should be noted that the SNR for OL tracking is expected to be 10–20% lower than for PLL tracking [Sokolovskiy *et al.*, 2006a] and that this study is based on internal bit removal, which may cause some errors in the lower tropical troposphere because of incorrect bit removal [Sokolovskiy *et al.*, 2006b]. The reduction in the measurement errors found below the top of the boundary layer merely reflects that the most noisy occultation does not penetrate into the boundary layer even for OL processing.

[64] Above approximately 30 km height, the largest errors are found at high latitudes and the smallest errors at low latitudes. This dependence with latitude is related to the residual ionospheric noise, which on an average increases with latitude [Lohmann, 2005].

[65] Below 20 and 25 km height, the dominant contribution to the total error is most likely model errors, particularly model representativeness errors, because of the fairly low horizontal and vertical resolution of the model. As the horizontal resolution of the model is comparable to the horizontal resolution of RO, there is hardly any contribution to the total errors related to the horizontal resolution of RO [Sokolovskiy *et al.*, 2005]. The contribution to the total errors from the lower vertical resolution of the model is particularly evident at the top of the planetary boundary layer and at the tropopause height.

[66] Generally, the measurement errors account for a considerable part of the total errors above 25 km, especially at high latitudes. The larger deviations between model and RO in the tropics and midlatitudes are probably related to gravity wave information contained in the RO observations that cannot be represented by the model as suggested by *Healy and Thépaut* [2006]. This is also consistent with the findings of *Marquardt and Healy* [2005] who concluded that, for realistic noise levels, fluctuations in RO profiles caused by gravity waves will be notably larger than fluctuations caused by measurement errors below approximately 30 km height. The increase in the total errors above 30 to 35 km height that cannot be accounted for by the increase in measurement error is probably related to an increase in the model errors with height.

[67] The total errors presented here have a large contribution from representativeness errors. Representativeness errors related to the lower vertical resolution of a model can easily be reduced in a data assimilation scheme by smoothing the RO data to the same vertical resolution as the model. However, the results presented here and the findings of *Healy and Thépaut* [2006] and *Marquardt and Healy* [2005] suggest that it may be advantageous to perform even stronger smoothing in the stratosphere to get rid of the gravity wave information. Whether stronger smoothing in the troposphere would be an advantage is currently not clear.

[68] For the model used in this study, there is hardly any contribution to the total error related to the RO horizontal resolution, however, for models with high horizontal resolutions (<100 km), the higher resolution of the model may result in considerable deviations between RO and the model [*Sokolovskiy et al.*, 2005]. For high-resolution models, these errors may be reduced by approximately a factor of 10 by applying so-called non-local observation operators [*Sokolovskiy et al.*, 2005; *Syndergaard et al.*, 2004, 2005]. In these cases, the measurement errors provide a lower bound for the maximum improvement that can be achieved with such operators.

[69] Finally, we note that the structure and magnitude of the measurement errors presented in this study are in fairly good agreement, though being a little smaller, with earlier studies based on CHAMP and SAC-C RO data [*Gorbunov et al.*, 2006; *Hajj et al.*, 2004; *Kuo et al.*, 2004], even though these studies are based on different processing strategies, data sets, and error estimation procedures.

4.2. Error Distributions

[70] Figures 7–9 depict the error distribution at different heights for both the fractional bending angle errors and the fractional refractivity errors for the tropics, midlatitudes, and the polar regions. These figures show that, for both refractivity and bending angle errors, the occultation-to-occultation variability generally spans one order of magnitude at all heights and latitudes. Moreover, the error distributions are not Gaussian at all and have long tails with outliers. It is also seen that the variability of the OL measurement errors is somewhat larger than the variability of the PLL measurement errors. As discussed above, this is most likely a result of the OL being able to track RO signals under atmospheric conditions for which the PLL fails. Below 20 km height, both GO and RH processing are used adding to the

occultation-to-occultation variability. The two single stems in the error distributions for 2 km height in Figure 7 merely reflect that only two PLL occultations penetrated to 2 km height in the tropics.

4.3. Error Autocorrelation Functions

[71] As the error characteristics are strongly dependent on whether the data are being processed using GO processing or RH processing, we will present error autocorrelation functions for the different processing modes rather than for different heights and latitudes. Additionally, for the RH processing error, autocorrelation functions are presented for $\text{SNR}_{\text{FSI}} > 5$ and for $\text{SNR}_{\text{FSI}} < 5$ for both OL and PLL. In all the cases, the bending angle error autocorrelation functions are computed as described in section 3 for each occultation. Subsequently, the mean bending angle error autocorrelation functions are computed from these autocorrelation functions.

[72] Because of the Abel integral, bending angle errors at high altitudes propagate to refractivity errors at lower heights. Therefore in this section, equation (15) is not used to compute the refractivity error autocorrelation functions. Instead, to prevent errors from the GO regions from influencing the computed refractivity error autocorrelation functions for the RH region and to prevent errors from the climate model from influencing the computed refractivity error autocorrelation functions for the GO region, the autocorrelation functions for the refractivity errors r_N are computed by convolving the mean bending angle error autocorrelation functions r_α with the magnitude of the impulse response H of the Abel transform:

$$r_N(\tau) = \int r_\alpha(x - \tau) |H(x)|^2 dx \quad (22)$$

H is derived in Appendix A.

[73] Figure 10 shows the normalized error autocorrelation functions for GO processing as well as for the two RH processing cases for both bending angles and refractivities. For RH processing, autocorrelation functions are shown for $\text{SNR}_{\text{FSI}} > 5$ and for $\text{SNR}_{\text{FSI}} < 5$. For the refractivities, the autocorrelation functions are computed for three different integration intervals, namely $a_1 - a_0 = 10$ km, 50 km, and 100 km. In Figure 10, the refractivity error autocorrelation functions are presented as a function of impact parameter in order to make them directly comparable with the bending angle error autocorrelation functions and to make the refractivity error autocorrelation functions independent of height. From Figure 10, it follows that the error correlation lengths for the bending angle errors are strongly related to the applied smoothing being approximately 1 km in the GO region and about 100 m in the RH region.

[74] The negative correlations in Figure 10 are a result of the differentiation involved in the retrievals, for example, differentiation of L1 and L2 phases for GO processing and differentiation of the FSI phase for RH processing. The negative correlation for the GO processing is somewhat smaller than the negative correlations reported by *Rieder and Kirchengast* [2001] and *Syndergaard* [1999]. This implies that the L1 and L2 phase noise is not white, as was assumed in those studies. For the RH processing, the OL and PLL error autocorrelation functions are remarkably

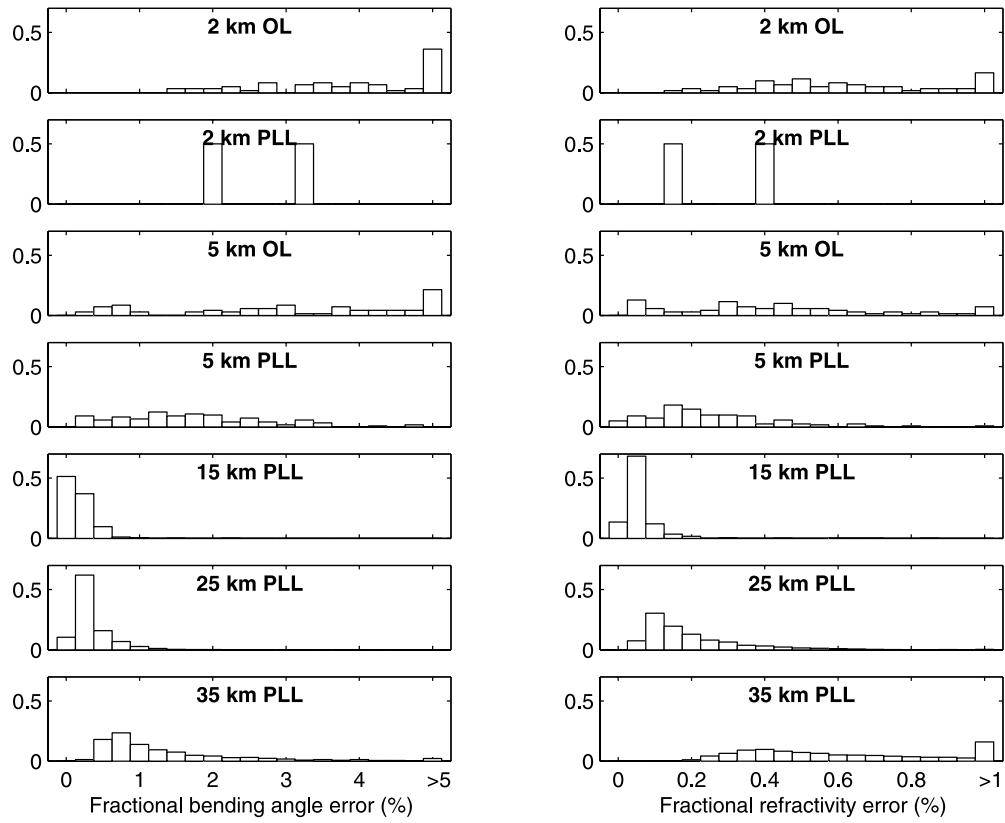


Figure 7. Low latitude error distributions. Left panel: fractional bending angle errors. Right panel: fractional refractivity errors.

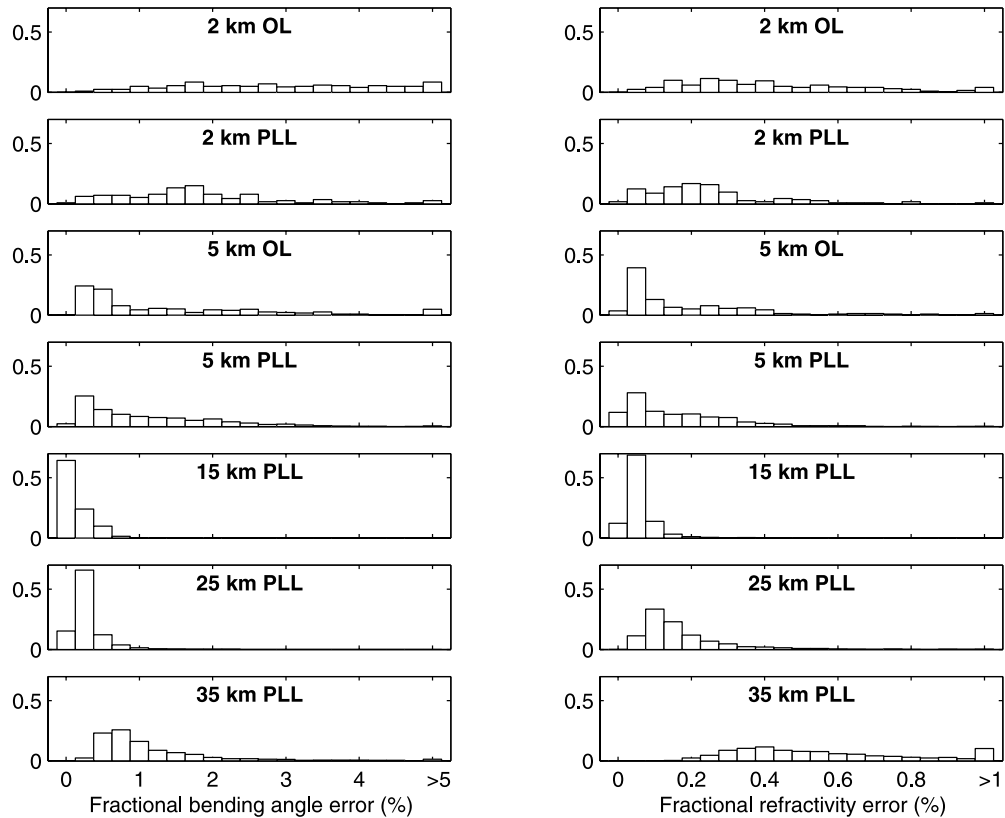


Figure 8. Midlatitude error distributions. Left panel: fractional bending angle errors. Right panel: fractional refractivity errors.

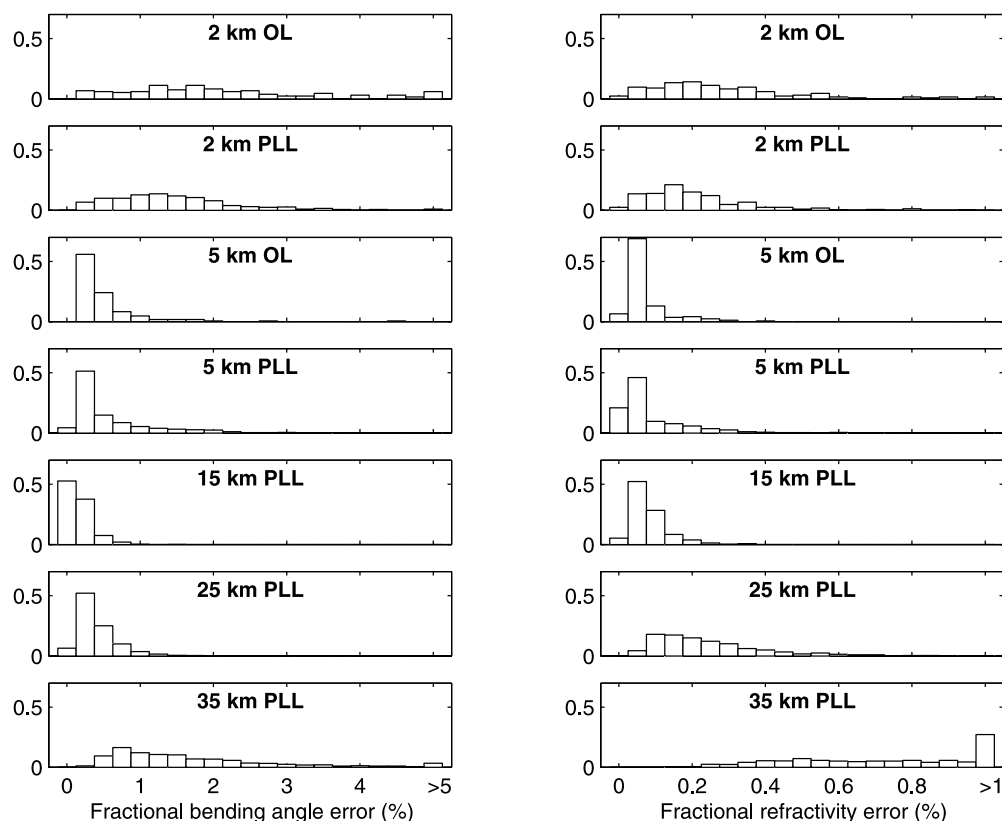


Figure 9. High latitude error distributions. Left panel: fractional bending angle errors. Right panel: fractional refractivity errors.

alike. The error correlation lengths for $\text{SNR}_{\text{FSI}} > 5$ and for $\text{SNR}_{\text{FSI}} < 5$ are similar, whereas the negative correlations for $\text{SNR}_{\text{FSI}} > 5$ are larger than for $\text{SNR}_{\text{FSI}} < 5$. It is not clear whether this difference is related to differences in the noise characteristics or whether it is related to some nonlinear effects in the noise propagation for $\text{SNR}_{\text{FSI}} < 5$.

[75] Autocorrelation functions for the refractivity errors are notably broader than for the bending angle errors. The GO processing results in the broadest autocorrelation functions, with a correlation coefficient of about 0.5 for a 10 km correlation lag except for the shortest integration interval. For the RH processing, the corresponding correlation coefficient is about 0.25–0.35 with the smallest correlations for $\text{SNR}_{\text{FSI}} > 5$. This is related to the slightly larger negative correlations for the bending angles errors for $\text{SNR}_{\text{FSI}} > 5$, which result in a narrower autocorrelation function than for $\text{SNR}_{\text{FSI}} < 5$, where the negative bending angle correlations are smaller.

5. Summary and Conclusions

[76] The resolution and the measurement error characteristics impose fundamental limits on the accuracy and precision to which atmospheric structures can be detected by the RO technique. The purpose of this study is to give a description of the RO measurement error characteristics based on an analysis of SAC-C OL and PLL occultation data processed by CDAAC. The CDAAC RO processing chain is based on geometrical optical (GO) processing at

high altitudes and radio holographic (RH) processing in the lower part of the atmosphere.

[77] The error characteristics have been computed by applying dynamic error estimation, where the errors are estimated on a profile-to-profile basis, which allows for computing error characteristics and for assessing the occultation-to-occultation measurement error variability.

[78] The mean error profiles show that the largest measurement errors are found in the lower troposphere, where the bending angle measurement errors are within the range from 1 to 6% whereas refractivity measurement errors are within the range from 0.2% to 1%.

[79] The measurement errors are the smallest in the height range between about 5–7 km and 20–25 km, about 0.2–1% for bending angles and 0.1–0.2% for refractivity at all latitudes for both OL (only relevant below 10 km) and PLL. Between approximately 20 and 40 km height, the fractional measurement errors increase almost exponentially to approximately 2.5–3% for bending angles and 0.8–1.1% for refractivity.

[80] Comparison between refractivity measurement errors and the deviations between retrieved refractivities and the ECMWF reanalysis showed that, for this particular model, the measurement errors constitute about 10–25% of the deviations below about 20–25 km height, whereas the measurement errors account for a considerable part of the deviations above 20–25 km height. Though our findings also indicate that, in the tropics and at midlatitudes, there is also a considerable contribution to the deviations from gravity waves in the lower stratosphere. Below 20–25 km,

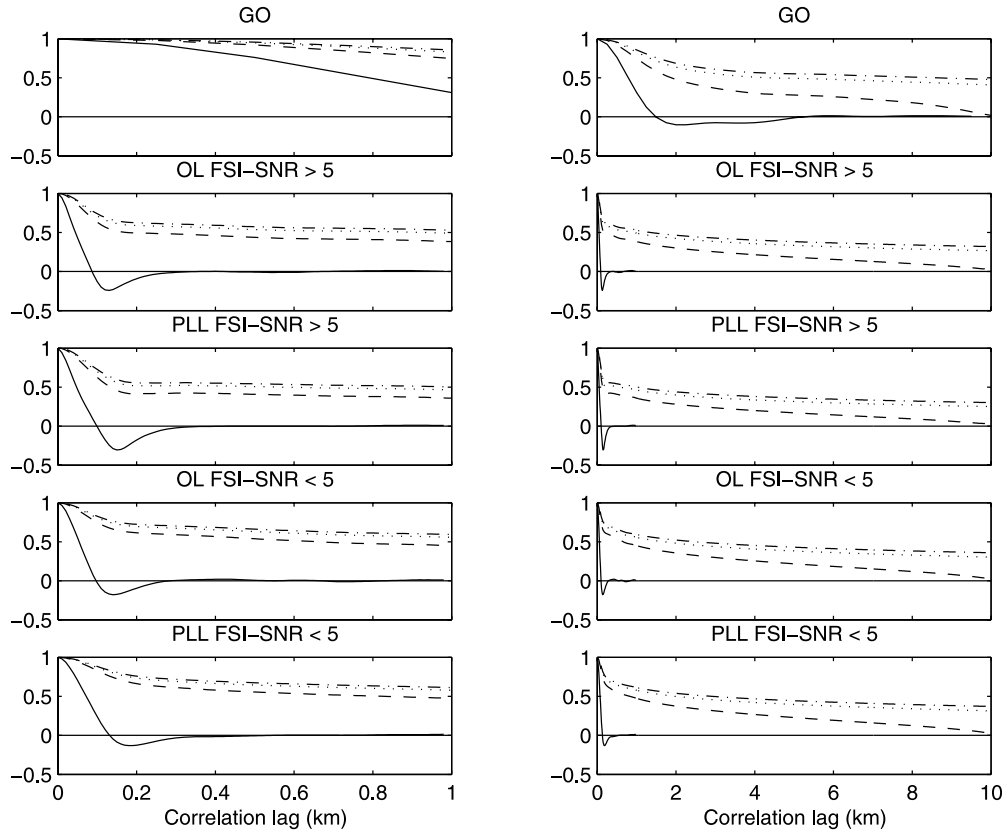


Figure 10. Normalized error autocorrelation functions: solid line: bending angle errors. Dashed line: refractivity errors 10-km integration interval. Dotted line: refractivity errors 50-km integration interval. Dash-dotted line: refractivity errors 100-km integration interval. Panels on the left show the same as panels on the right, except that in the left panels the correlation lag range is restricted to 0–1 km.

the dominant contribution to the deviations is expected to be model errors, in particular, model representativeness errors.

[81] Generally, it is found that the magnitude of the measurement errors varies considerably from occultation to occultation. Both bending angle and refractivity measurement errors were found to span approximately one order of magnitude at all heights and latitude bands. The variability and the magnitude of OL measurement errors are larger than for PLL measurement errors; this is attributed to the ability of OL tracking to track RO signals under atmospheric conditions for which the PLL tracking fails.

[82] Error autocorrelation functions for both GO and RH processing have been computed, and it was found that the error correlation lengths are strongly related to the characteristics of the noise smoothing filter. For the GO and the RH processing, the bending angle error correlation length is about 1 km and 100 m, respectively, and corresponds approximately to the cutoff frequency of the applied noise filter. The widths of the refractivity error correlation functions are notably broader than for the bending angle error correlation functions. Only small differences were found between the autocorrelation functions for OL data and the PLL data.

Appendix A

[83] The magnitude response for the Abel transform can be computed from the frequency response of the Abel

transform F which may be approximated as [Lohmann, 2005]:

$$F(k) = \exp(ika_0) \frac{10^6}{\sqrt{\pi k a_0}} \times \left[C\left(\sqrt{\frac{2}{\pi}} k(a_1 - a_0)\right) + iS\left(\sqrt{\frac{2}{\pi}} k(a_1 - a_0)\right) \right] \quad (\text{A1})$$

In equation (A1), a_0 and a_1 are, respectively, the smallest and the largest impact parameter used in the Abel integral and $C(x)$ and $S(x)$ are the Fresnel cosine and sine integrals defined as:

$$C(x) = \int_0^x \cos\left(\frac{\pi v^2}{2}\right) dv, \quad S(x) = \int_0^x \sin\left(\frac{\pi v^2}{2}\right) dv \quad (\text{A2})$$

As $|F|^2$ is an even function, the magnitude of the Abel transform impulse response may be computed as:

$$|H(\tau)|^2 = 2 \int_0^{k_{\max}} \cos(\tau k) |F(k)|^2 dk \quad (\text{A3})$$

Here k_{\max} is the largest wave number as defined by the sampling frequency of the bending angle profile. By intro-

ducing the dimensionless wave number k' and correlation lag τ' ,

$$k' = \frac{a_1 - a_0}{2\pi k}, \quad \tau' = \frac{\tau}{a_1 - a_0} \quad (\text{A4})$$

equation (A3) may be expressed as:

$$|H(\tau)|^2 = |H'(\tau')|^2 = \frac{2 \times 10^{12}}{\pi k a_0} \int_0^{k'_{\max}} \frac{\cos(2\pi\tau'k')}{k'} \cdot \left[(C(2\sqrt{k'}))^2 + (S(2\sqrt{k'}))^2 \right] dk' \quad (\text{A5})$$

where it has been implicitly assumed that the impulse response for the Abel transform is constant with height, which is of course an approximation. However, the impulse response for the Abel transform varies slowly with height.

[84] **Acknowledgments.** The author is grateful to Doug Hunt (UCAR), without his help with the CDAAC database this work would not have been possible, and to Sergey Sokolovskiy (UCAR) and Stig Syndergaard (UCAR) for valuable discussions about this study. Two anonymous reviewers' constructive comments and suggestions to the manuscript are also greatly appreciated.

[85] This work was supported by National Environmental, Satellite, Data, and Information Service (NESDIS).

References

- Ao, C. O., et al. (2003), Lower-troposphere refractivity bias in GPS occultation retrievals, *J. Geophys. Res.*, 108(D18), 4577, doi:10.1029/2002JD003216.
- Beyerle, G., et al. (2003), Simulation studies of GPS radio occultation measurements, *Radio Sci.*, 38(5), 1084, doi:10.1029/2002RS002800.
- de la Torre, A., and P. Alexander (2005), Gravity waves above Andes detected from GPS radio occultation temperature profiles: Mountain forcing?, *Geophys. Res. Lett.*, 32, L17815, doi:10.1029/2005GL022959.
- Fjeldbo, G., et al. (1971), The neutral atmosphere of Venus studied with the Mariner V radio occultation experiments, *Astron. J.*, 76, 123–140.
- Gobiet, A., et al. (2005), Climatological validation of stratospheric temperatures in ECMWF operational analyses with CHAMP radio occultation data, *Geophys. Res. Lett.*, 32, L12806, doi:10.1029/2005GL022617.
- Gobiet, A., and G. Kirchengast (2004), Advancement of Global Navigation Satellite System radio occultation retrieval in the upper stratosphere for optimal climate monitoring utility, *J. Geophys. Res.*, 109, D24110, doi:10.1029/2004JD005117.
- Gorbunov, M. E. (2002a), Canonical transform methods for processing radio occultation data in the lower troposphere, *Radio Sci.*, 37(5), 1076, doi:10.1029/2000RS002592.
- Gorbunov, M. E. (2002b), Ionospheric correction and statistical optimization of radio occultation data, *Radio Sci.*, 37(5), 1084, doi:10.1029/2002RS002370.
- Gorbunov, M. E., and L. Kornbluh (2003), Analysis and validation of Challenging Minisatellite Payload (CHAMP) radio occultation data, *J. Geophys. Res.*, 108(D18), 4584, doi:10.1029/2002JD003175.
- Gorbunov, M. E. et al. (1996), Advanced algorithms of inversion of GPS/MET satellite data and their application to reconstruction of temperature and humidity, *Scientific Report 211*, Max-Planck-Institut für Meteorologie, Hamburg.
- Gorbunov, M. E., et al. (2004), Comparative analysis of radio occultation processing approaches based on Fourier integral operators, *Radio Sci.*, 39, RS6004, doi:10.1029/2003RS002916.
- Gorbunov, M. E., et al. (2006), Radio holographic filtering, error estimation, and quality control of radio occultation data, *J. Geophys. Res.*, 111, D10105, doi:10.1029/2005JD006427.
- Hajj, G. A., et al. (2002), A technical description of atmospheric sounding by GPS occultation, *J. Atmos. Sol.-Terr. Phys.*, 64, 451–469.
- Hajj, G. A., et al. (2004), CHAMP and SAC-C atmospheric occultation results and intercomparisons, *J. Geophys. Res.*, 109, D06109, doi:10.1029/2003JD003909.
- Healy, S. B. (2001), Smoothing radio occultation bending angles above 40 km, *Ann. Geophys.*, 19, 459–468.
- Healy, S. B., et al. (2005), Forecast impact experiment with GPS radio occultation measurements, *Geophys. Res. Lett.*, 32, L03804, doi:10.1029/2004GL020806.
- Healy, S. B., and J.-N. Thépaut (2005), 4D-Var assimilation experiment with CHAMP GPS radio occultation measurements, *Geophys. Res.*, 7, 031147.
- Healy, S. B., and J.-N. Thépaut (2006), Assimilation experiment with CHAMP GPS radio occultations measurements, *Q. J. R. Meteorol. Soc.*, 132, 605–623.
- Jensen, A. S., et al. (2003), Full spectrum inversion of radio occultation signals, *Radio Sci.*, 38(3), 1040, doi:10.1029/2002RS002763.
- Kuo, Y.-H., et al. (2004), Inversion and error estimation of GPS radio occultation data, *J. Meteorol. Soc. Jpn.*, 82, 507–531.
- Kursinski, E. R., and G. A. Hajj (2001), A comparison of water vapor derived from GPS occultations and global weather analyses, *J. Geophys. Res.*, 106, 1113–1138.
- Kursinski, E. R., et al. (1997), Observing Earth's atmosphere with radio occultation measurements using the Global Positioning System, *J. Geophys. Res.*, 102, 23,429–23,465.
- Kursinski, E. R., et al. (2000), The radio occultation technique, *Terr. Atmos. Oceanic Sci.*, 11, 53–114.
- Ladreiter, H. P., and G. Kirchengast (1996), GPS/GLONASS sensing of the neutral atmosphere: Model-independent correction of ionospheric influence, *Radio Sci.*, 31, 877–891.
- Lohmann, M. S. (2005), Application of dynamical error estimation for statistical optimization of radio occultation bending angles, *Radio Sci.*, 40, RS3011, doi:10.1029/2004RS003117.
- Lohmann, M. S. (2006), Dynamic error estimation for radio occultation bending angles retrieved by the FSI technique, *Radio Sci.*, 41, RS5005, doi:10.1029/2005RS003396.
- Marquardt, C., and S. B. Healy (2005), Notes and correspondence: Measurement noise and stratospheric gravity waves characteristics obtained from GPS occultation data, *J. Meteorol. Soc. Jpn.*, 83, 417–428.
- Marquardt, C., et al. (2001), An assessment of the quality of GPS/MET radio limb soundings during February 1997, *Phys. Chem. Earth, Part A*, 3, 125–130.
- Melbourne, W. G. et al. (1994), The application of spaceborne GPS to atmospheric limb sounding and global change monitoring, Jet. Propul. Lab., Pasadena, Calif.
- Miller, K. S., and M. M. Rochwarger (1972), A covariance approach to spectral moment estimation, *IEEE Trans. Inf. Theory*, IT-18, 588–596.
- Randel, W. et al. (2002), SPARC Report No. 3: SPARC Intercomparison of Middle Atmosphere Climatologies, WCCRP No. 116, WMO/TD No. 1142, WMO/ICSU/IOC WorldClimate Research Program.
- Ratnam, M. V., et al. (2004), Global and seasonal variation of stratospheric gravity wave activity deduced from CHAMP/GPS satellite, *J. Atmos. Sci.*, 61, 1610–1620.
- Rieder, M., and G. Kirchengast (2001), Error analysis and characterization of atmospheric profiles retrieved from GNSS occultation data, *J. Geophys. Res.*, 106, 31,755–31,770.
- Rocken, C., et al. (1997), Analysis and validation of GPS/MET data in the neutral atmosphere, *J. Geophys. Res.*, 102, 29,849–29,866.
- Schmidt, T., et al. (2005), GPS radio occultation with CHAMP and SAC-C: Global monitoring of thermal tropopause parameters, *Atmos. Chem. Phys.*, 5, 1473–1488.
- Schmidt, T., et al. (2006), A climatology of multiple tropopauses derived from GPS radio occultations with CHAMP and SAC-C, *Geophys. Res. Lett.*, 33, L04808, doi:10.1029/2005GL024600.
- Schröder, T., et al. (2003), Validating the microwave sounding unit stratospheric record using GPS occultations, *Geophys. Res. Lett.*, 30(14), 1734, doi:10.1029/2003GL017588.
- Sokolovskiy, S. (2001), Tracking tropospheric radio occultation signals from low Earth orbit, *Radio Sci.*, 36, 483–498.
- Sokolovskiy, S. (2003), Effect of superrefraction on inversions of radio occultation signals in the lower troposphere, *Radio Sci.*, 38(3), 1058, doi:10.1029/2002RS002728.
- Sokolovskiy, S. (2004), Open loop tracking and inverting GPS L1 radio occultation signals: Simulation study, paper presented at First international workshop on occultations for atmosphere and climate, Springer, New York.
- Sokolovskiy, S., and D. Hunt (1996), Statistical optimization approach for GPS/MET data inversion, paper presented at Second international URSI GPS/MET workshop, Union of Radio Sci. Int., Tucson, Ariz.
- Sokolovskiy, S., et al. (2005), Assessing the accuracy of a linearized observation operator for assimilation of radio occultation data: Case simulation with a high resolution weather model, *Mon. Weather Rev.*, 133, 2112–2200.
- Sokolovskiy, S., et al. (2006a), Monitoring the atmospheric boundary layer by GPS radio occultation signals recorded in open-loop mode, *Geophys. Res. Lett.*, 33, L12813, doi:10.1029/2006GL025955.
- Sokolovskiy, S., et al. (2006b), GPS profiling of the lower troposphere from space: Inversion and demodulation of the open-loop radio occultation signals, *Geophys. Res. Lett.*, 33, L14816, doi:10.1029/2006GL026112.

- Spilker, J. J. (1980), GPS signal structure and performance characteristics, in *Global Positioning System*, edited, pp. 29–54, The Inst. of Navig., Alexandria, VA.
- Steiner, A. K., and G. Kirchengast (2005), Error analysis for GNSS radio occultation data based on ensembles of profiles from end-to-end simulations, *J. Geophys. Res.*, *110*, D15307, doi:10.1029/2004JD005251.
- Steiner, A. K., et al. (1999), Inversion, error analysis, and validation of GPS/MET data, *Ann. Geophys.*, *17*, 122–138.
- Stephens, S. A., and J. B. Thomas (1995), Controlled-root formulation for digital phase-locked loops, *IEEE Trans. Aerosp. Electron. Syst.*, *31*, 78–95.
- Syndergaard, S. (1999), Retrieval analysis and methodologies in atmospheric limb sounding using the GNSS occultation technique, *DMI Scientific Report 99-6* (Available at <http://www.dmi.dk/dmi/sr99-6.pdf>), Danish Meteorological Institute, Copenhagen.
- Syndergaard, S. et al. (2004), Assimilation of radio occultation data into atmospheric models, paper presented at Atmosphere and climate: studies by occultation methods—Proceedings from second international workshop on occultations for atmosphere and climate (OPAC-2), Springer, New York 13 Sep–17 Sep.
- Syndergaard, S., et al. (2005), A refractive index mapping operator for assimilation of occultation data, *Mon. Weather Rev.*, *133*, 2650–2668.
- Tsuda, T., and K. Hocke (2004), Application of GPS radio occultation data for studies of atmospheric waves in the middle atmosphere and ionosphere, *J. Meteorol. Soc. Jpn.*, *82*, 419–426.
- Vorob'ev, V. V., and T. G. Krasil'nikova (1994), Estimation of the Doppler shift measurements at frequencies used in the NAVSTAR system, *Izv. Russ. Acad. Sci. Atmos. Oceanic Phys.*, *29*, 602–609.
- Zou, X., et al. (2004), Impact of CHAMP radio occultation observations on global analysis and forecasts in the absence of AMSU radiance data, *J. Meteorol. Soc. Jpn.*, *82*, 533–549.

M. S. Lohmann, Teklatech A/S, Diplomvej, Bygning 377, DK-2800, Lyngby, Denmark. (martin@teklatech.com)